REPORT DOCUMENTATION PAGE

AFRL-SR-BL-TR-01-

OC87

1. AGENCY USE ONLY *(Leave blank)*	2. REPORT DATE 29 December 2000	3. REPORT TYPE AND DATES COVERED Final 1 July 97 – 30 June 00	
4. TITLE AND SUBTITLE USE OF MEMS FOR MICRO AIR VEHICLES		5. FUNDING NUMBERS F49620-97-1-0507	
6. AUTHORS Bruce Carroll, Norman Fitz-Coy, Wei Shyy, Toshikazu Nishida			
7. PERFORMING ORGANIZATION NAME(S) AND ADDRESS(ES) University of Florida 231 Aerospace Building Gainesville FL 32611		8. PERFORMING ORGANIZATION REPORT NUMBER	
8. SPONSORING/MONITORING AGENCY NAME(S) AND ADDRESS(ES) Air Force Office of Scientific Research 801 North Randolph Street Arlington VA 22203		10. SPONSORING/MONITORING AGENCY REPORT NUMBER	

11. SUPPLEMENTARY NOTES

AIR FORCE OFFICE OF SCIENTIFIC RESEARCH (AFOSR)
NOTICE OF TRANSMITTAL DTIC. THIS TECHNICAL REPORT
HAS BEEN REVIEWED AND IS APPROVED FOR PUBLIC RELEASE
LAW AFR 190-12. DISTRIBUTION IS UNLIMITED.

12a. DISTRIBUTION/AVAILABILITY STATEMENT

Approved for Public Release

12b. DISTRIBUTION CODE

13. ABSTRACT *(Maximum 200 words)*

This report summarizes final results from a multidisciplinary effort to investigate the application of MEMS to the control of low Reynolds number flows about Micro Air Vehicles (MAVs). The specific goals of this investigation were to develop a quantitative and qualitative understanding of microelectromechanical systems (MEMS) based sensor and actuator interactions with low Reynolds number flows found on MAVs, resulting in improved aerodynamic performance and mechanisms for active and passive flight control. The detailed results are made available in various publications which are summarized here.

14. SUBJECT TERMS		15. NUMBER OF PAGES 12
20010220 008		16. PRICE CODE

17. SECURITY CLASSIFICATION OF REPORT Unclassified	18. SECURITY CLASSIFICATION OF THIS PAGE Unclassified	19. SECURITY CLASSIFICATION OF ABSTRACT Unclassified	20. LIMITATION OF ABSTRACT UL

USE OF MEMS FOR MICRO AIR VEHICLES

FINAL TECHNICAL REPORT

Bruce Carroll, Norman Fitz-Coy, and Wei Shyy
Department of Aerospace Engineering, Mechanics & Engineering Science
University of Florida

Toshikazu Nishida
Department of Electrical and Computer Engineering
University of Florida

Abstract

This report summarizes final results from a multidisciplinary effort to investigate the application of MEMS to the control of low Reynolds number flows about Micro Air Vehicles (MAVs). The specific goals of this investigation were to develop a quantitative and qualitative understanding of microelectromechanical systems (MEMS) based sensor and actuator interactions with low Reynolds number flows found on MAVs, resulting in improved aerodynamic performance and mechanisms for active and passive flight control. The detailed results are made available in various publications which are summarized here.

Approach

A dominant aerodynamic feature of MAVs is the lower lift-to-drag ratio and much reduced stall margin, which leads to a precipitous decline in aerodynamic efficiency as Reynolds number is lowered. The amplification of small-scale MEMS control inputs into large-scale effects via fluid dynamic instability and growth mechanism are being investigated. Figure 1 shows a low Reynolds number (Re < 100,000), laminar separation followed by transition of the separated shear layer and reattachment. Mild actuation of the boundary layer near the separation location is expected to trigger a quicker transition of the separated shear layer, providing a mechanism for control of the reattachment location. We are also considering MEMS induced and controlled vortical structures, originating with small perturbations at the leading edge of the MAV wing to enhance
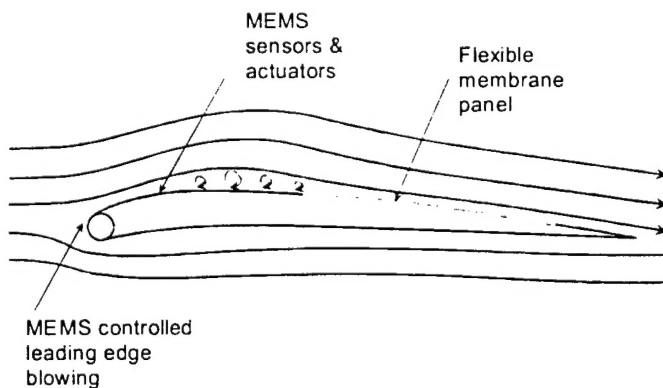

Fig. 1. Illustration of actuation and sensing strategies

the lift. A third possible mechanism is to utilize flexible membrane wing panels as an additional amplification mechanism for the MEMS actuation. While Figure 1 describes our ultimate goal for an improved MAV airfoil, a simpler geometry is being employed to study the fluid/MEMS interactions from both a fundamental fluid dynamics perspective and from a control theory viewpoint.

Our test configuration is shown in Figure 2. This configuration consists of a "macro" scale vibrating piezo flap for actuation and a MEMS based shear sensor array for reattachment detection. As discussed below, we are using this configuration to quantify the MEMS actuation requirements, to develop our MEMS sensing capabilities and to provide a test case for development of model based and neural network control strategies for the non-linear system.

Fig. 2. Test Geometry for quantitative determination of actuation requirements.
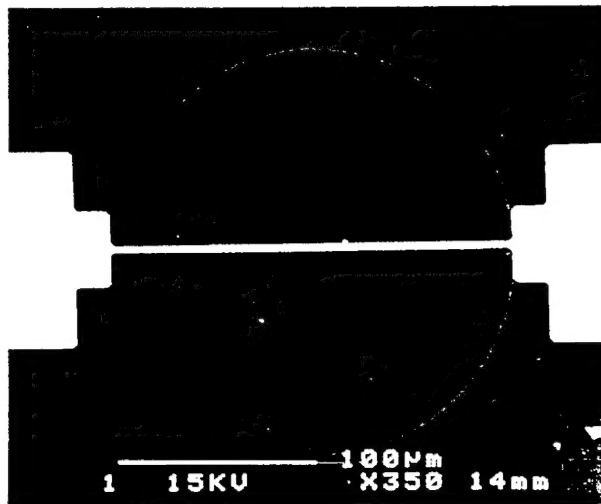
Fig 3. SEM image of MEMS shear sensing element.

Results
Thermal Shear Stress Sensor

The thermal shear stress sensor utilized in this investigation is shown in the SEM photograph of Figure 3. The sensor consists of a 0.15 µm-thick x 200 µm-long x 4 µm-wide thin-film platinum sensing element constructed over a vacuum cavity sealed by a 150 Angstrom-thick silicon-nitride membrane. Each sensor possesses two gold leads at each end of the sensing element. The details of the device design, fabrication, and characterization are given by Cain (2000). In summary, the sensor was characterized in a Constant current mode of operation for both static and dynamic conditions. The static sensitivity was measured with a laminar flow cell for thermal overheats of 0.2 to 1.0 and wall shear stresses from 0 Pa to 1.7 Pa. The static sensitivity increased with higher thermal overheat with a maximum sensitivity of 11 mV/Pa at an overheat ration of 1.0. Dynamic
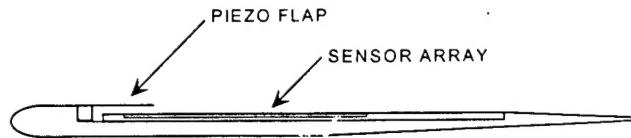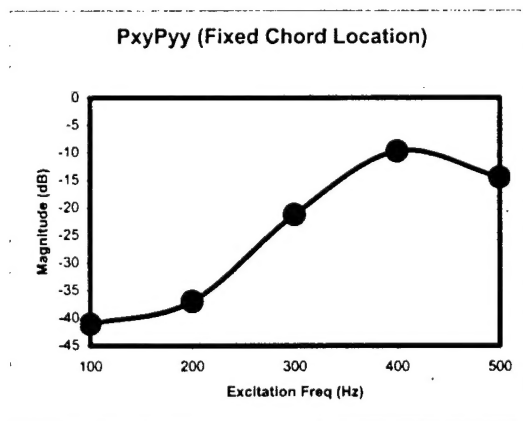

Fig. 4. Signal output from MEMS sensor element

wall shear stress sensitivities were obtained at multiple mean shear stress levels and overheats, using a novel in-situ dynamic calibration technique. This technique provides known sinusoidal shear-stress perturbations generated via acoustic plane-wave excitation. The sensor exhibited approximately a 40 dB/decade roll-off with a corner frequency of 600 Hz, indicating a highly damped 2nd order system. The pressure sensitivity of the sensor was found to be negligible and the noise floor spectra at zero mean flow and multiple overheats were also experimentally determined to be < 100 nV/Hz. Note that the calibration of the thermal sensor depends on the flow temperature. The dynamic calibration is further complicated by the frequency dependent heat conduction into the supporting structure. The difficulties associated with the conjugated heat-transfer processes preclude a thorough understanding of the frequency response function. As a consequence, the use of these sensors for quantitative shear measurements is limited. However, their utility as qualitative flow sensors for providing feedback to flow control devices is demonstrated.

The raw voltage signal from the MEMS sensors was not particularly useful as a feedback signal. However, the power spectrum at a fixed sensor location did give a useable output signal as shown in Fig. 4.

Airfoil Model

The zero-camber airfoil model is shown schematically in Figure 2. Photographs of the model are shown in Figure 5. The leading edge is an elliptic profile designed to prevent separation as would be found on a circular profile. A flap actuator is embedded in the upper surface with the trailing edge of the flap forming a step expansion where laminar flow separation occurs. The flow then reattaches to a flat surface in which pressure taps are embedded. The actuator flap consists of a brass shim, 51 mm wide by 16 mm chord length. The shim is cold-soldered to a brass block for surface mounting. A piezo ceramic is bonded to the shim using non-conducting epoxy. The shim is connected to ground and a voltage is applied to the piezo ceramic. Under this electrical stimulation, the piezo will deform leading to a concentrated bending moment at the piezo-shim interface. The airfoil chord is 137.2 mm (5.4 in.) and the distance from the leading edge to the trailing edge of the flap is 28.76 mm (1.125 in.). The step height is 1.4 mm.
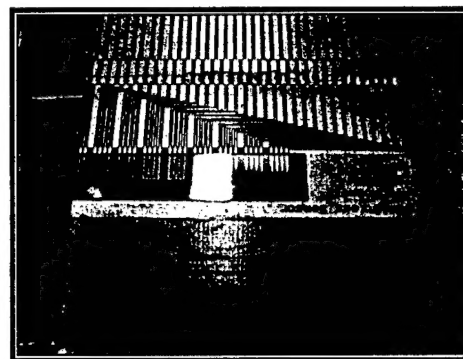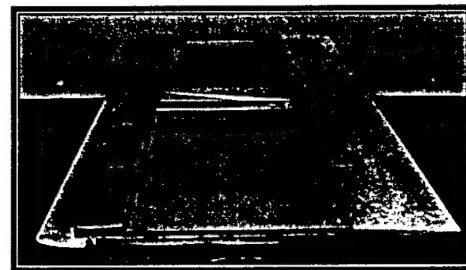

Fig. 5 Photographs of airfoil model showing actuator flaps and MEMS sensor array.

Laser Vibrometer

An interferometric technique to measure normal velocities of a vibrating surface was employed to quantitatively determine the deformation of the actuator flap. An incident helium-neon laser beam is focused on a particular point of the vibrating flap. The light scattered from the surface is detected by an interferometer. A Doppler shifted interference signal is generated due to the time varying difference between the incident and reflected beams. A photo-detector converts this interference signal to a voltage-time history, which is proportional to the time varying normal velocity of the surface. Integration of the velocity data gives the position of the surface. The response of the piezo-actuator system to a range of input frequencies was quantified as described next.

An excitation chirp signal was generated with a function generator. The chirp signal spanned a frequency range (desired bandwidth) from 0.1 Hz to 1000 Hz with amplitude of 250 mV. This signal was then amplified by a gain of 150 before application to the piezo. The period of the chirp was 0.8 seconds to give the desired number of FFT lines in the bandwidth for the spectral analysis of the vibrometer output. The input signal and the vibrometer output signal were digitized with a 16-bit data acquisition system. The analog anti-aliasing filter in the vibrometer was set to 5 kHz (cut-off) with a roll-off rate of −160 dB/sec. The stop-band (-80 dB) is approximately 8.8 kHz. The data was sampled at 10.24 kHz then digitally filtered and decimated to a lower record length to give the desired digital FFT resolution or lines.

Piezo-Actuator Characterization

Laser vibrometer measurements were made at the tip of the piezo-actuator (flap). The frequency response and phase of the linear system is shown in Fig 6. Note that the gain in the frequency response graph is based on the input voltage before the amplifier and the output tip velocity. The resonance frequency occurs at 700 Hz. Thus, the maximum possible tip velocity is about 820 mm/s (2.0 m/s/volts × 0.41 volts) with a corresponding deflection of about 186 μm. (The tip deflection is the integral of the sinusoidal tip velocity, i.e. tip deflection = tip velocity / $2\pi f$.) At 200Hz, the maximum tip velocity is 29.3 mm/s with a corresponding maximum deflection of 23.3 μm. A small phase shift occurs even at low frequencies. The phase is measured between the input sinusoidal signal and the output tip velocity (a cosine function). Thus the phase based on the tip deflection (a sine function) would be that shown plus 90°. Measurements of the transfer function were performed both with and without the free steam flow. There was no measurable difference between the unloaded wind-off case and the loaded
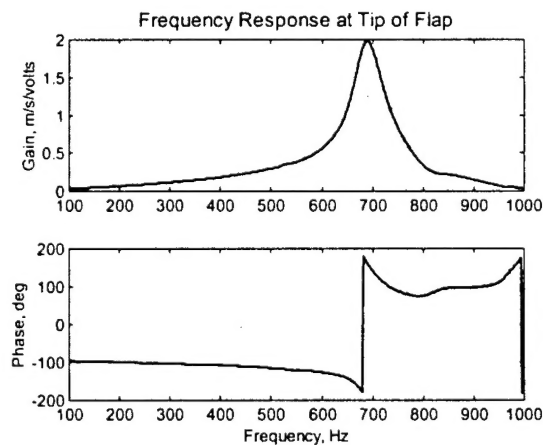

Fig. 6 Transfer function and phase shift of piezo-acutator tip velocity relative to input voltage signal.

wind-on case. This indicates that the aerodynamic loading effects on the actuator are negligible, at least at zero angle-of-attack.

Mean Pressure Distribution

For the pressure and velocity results presented, the airfoil was at zero angle-of-attack. The free stream velocity was 8.4 m/s and the Reynolds number was 79,000 based on the chord and 16,000 based on the distance from the leading edge to the separation location (i.e. the piezo-actuator tip). In the figures which follow, the origin (x = 0.0) is located at the trailing edge of the flap.

Wall mean pressure measurements were made on the upper airfoil surface. A single transducer was manually

Fig. 7. Mean surface pressure distributions on airfoil upper surface without excitation and with 200 Hz excitation.

scanned between the pressure ports. This transducer has an accuracy of 0.00035 inches of water. The estimated uncertainty in C_P was ± 0.02. The time constant for the measurements was on the order of 5 seconds. This was due both to the damping effect of the vinyl tubing connecting the pressure taps to the transducer and also to the inherent time response of the transducer itself. The mean surface pressure distributions shown in Figure 7 give a gross indication of the impact of the actuator on the flow. The flow separates at the backward facing step (i.e. flap) located at x = 0.0 mm. A local minimum in the Cp distribution indicates flow reattachement. The reattachment location is approximately 32 mm and 19 mm for no excitation and 200 Hz excitation, respectively.
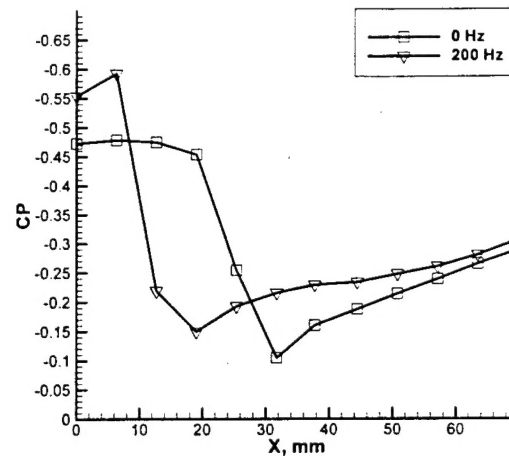
PIV

A digital, particle image velocimetry system was used to acquire instantaneous velocity fields between the actuated flap's tip and the average re-attachment point on the top surface of the airfoil. The computer-controlled PIV system consisted of a high resolution (1K x 1K) PIVCAM 10-30 CCD camera capable of 30 frames per second, a dual mini YAG laser (flashlamp-pumped) system with 50 mJ per pulse at 15 Hertz and a synchronizer for correct sequence and timing. Trigger signal outputs from the synchronizer control the laser's pulsing sequence so that the laser pulses are located in the appropriate video frames. All acquisition and analysis parameters are programmed via a Windows NT® program. A micro-processor controlled fogging unit with a distributor seeded the air flow at the inlet of the wind tunnel. Since a dual frame cross-correlation technique was used, no image shifting was required for directional ambiguity. The Table 1 summarizes the PIV settings. To capture the evolution of flow structures in the flow field, the PIV system was phase-locked to the excitation signal of the actuated flaps at 200 Hz. A PC based data acquisition/driver card with a circular buffer provided the proper timing of the TTL trigger and the excitation signal for the synchronizer and

flaps, respectively. The frequency of the trigger signal was set at a rate below the maximum acquisition rate of the PIV system

Mean Velocity Distributions

Fig. 8 shows two examples of the images captured by the PIV system. The top image is with no excitation (i.e. 0 Hz) and the bottom image is with 200 Hz excitation. Without excitation, the shear layer is seen to slowly grow in size and reattach to the upper surface. When excitation is applied, vortex structures are generated in the flow and are convected downstream. For sufficiently high excitation amplitude, the vortex shedding is periodic and correlated to the input oscillation. At lower amplitudes the vortex structure is more random and is not correlated to the flap motion.

Each of the images in Fig. 8 are actually a single image from an image pair. Using standard PIV data reduction procedures, the image pairs are correlated to each other to determine the velocity field at a single instance in time. The mean velocity field was then obtained by averaging between 80 to 100 of these individual realizations. The running average of the velocity at each spatial location was also computed and the number of points in the average was found to be sufficient for the average to reach an asymptotic value. The mean velocity distributions were obtained by averaging two types of measurements: 1) random measurements (taken at random time delays relative to the start of the sinusoidal actuator excitation signal) and 2) conditionally sampled measurements (taken at a particular time delay relative to the start of the excitation).

The results for the random averages are shown in Figure 9. As

| Table 1 PIV Settings	
YAG laser:	
Pulse separation time:	29.5μs
Pulse rate:	15 Hz (max), 10 Hz (phase-locked)
Pulse energy:	50mJ per pulse
Video camera:	
Field of view:	30.9 mm by 30.9 mm
Calibration scale:	30.88 μm per pixel
Frame rate:	30 Hz
f-stop:	5.6
Image analysis:	
Interrogation spot size:	32 pixels or 0.99 mm
Aspect ratio of int. spot size:	0.5
Cross-correlation computation:	via FFT
Peak search method:	Gaussian
Velocity filter:	Gaussian weighted average
Seeding:	
Fog unit:	Martin or LeMaitre fogger
Fog fluid:	Polyfuntional alcohol or Dipropylene glycol
Vapor density:	>1

1/2 in. scale
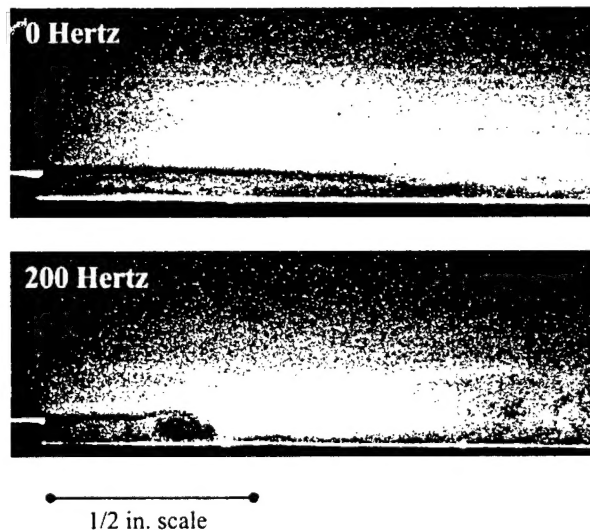
Fig. 8 Flow visualization using the PIV system. Top picture shows flow without excitation, bottom picture shows vortex structure generated at 200 Hz excitation.

expected this type of averaging masks the actual vortex structure in the 200 Hz case. In a time mean sense, the reattachment location is observed to move toward the step as excitation frequency is increased. This is consistent with the mean surface pressure results in Fig. 7. It is difficult to determine the exact reattachment location from the PIV images since velocity measurements do not extend all the way to the solid surface. This is due to problems in performing the spatial correlations when a portion of the interrogation region overlaps a stationary feature.

Tracking the vortex structures required that the PIV data be conditionally sampled. Multiple PIV velocity fields were measured at the pre-selected flap locations illustrated in Fig. 10. The trigger signal was actually based on the input waveform to the amplifier (actuator), which correspond to particular tip deflections. The resulting conditionally sampled mean velocity fields are presented in Fig. 11. Details about the trigger locations and the vortex locations are given in Table 2. Looking at Fig. 7 a) we see a vortex located at x = 8.9 mm. (The vortex location is the center of the vortex as determined by visual inspection of the stream function plots.) As time progresses, the vortex moves downstream. In Fig. 7 c) the vortex is located at x = 10.7 mm and has begun to appear distinct from the recirculation region just downstream of the step. The vortex continues to move downstream and the size of the recirculation region after the step grows. At the end of the sequence of images, a second vortex is not observed. Measurements later in the excitation cycle are required to detect
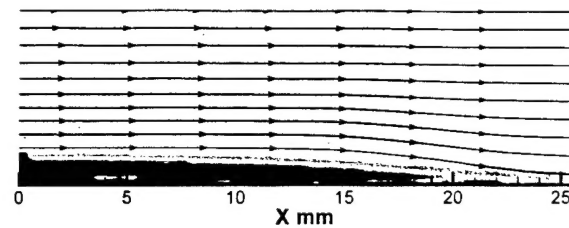
a) no excitation (0 Hz)
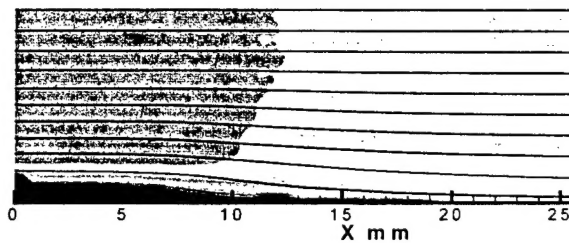
b) 200 Hz excitation

Fig. 9 Mean velocity profiles downstream of sudden expansion. Random phase shifts between realizations. The reattachment location is seen to move forward with excitation but time dependent flow structures are obscured by the random averaging procedure.
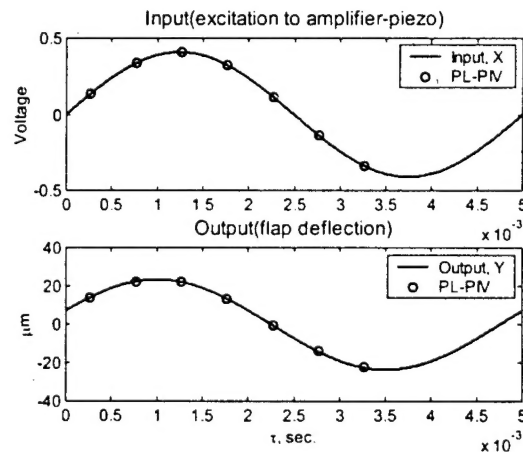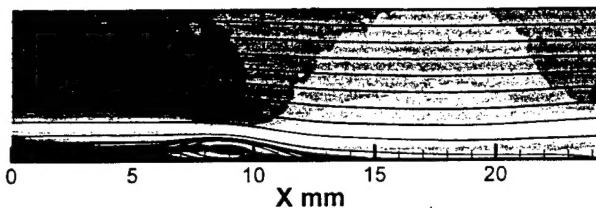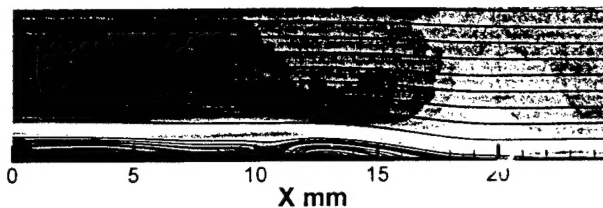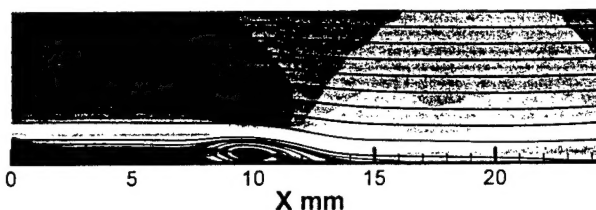

Fig. 10 Trigger points for the conditionally sampled PIV images shown on both the input waveform to the actuators and on the output deflection waveform for the actuators
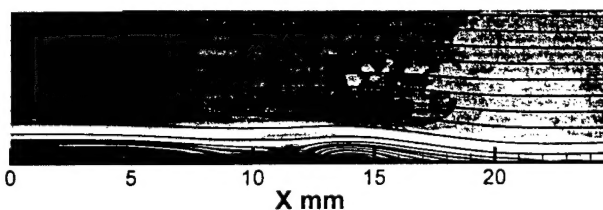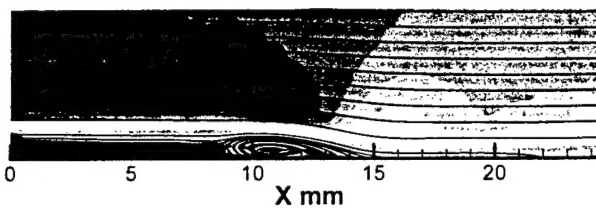
a) 5.4% of input waveform, flap deflection = 14.1µm
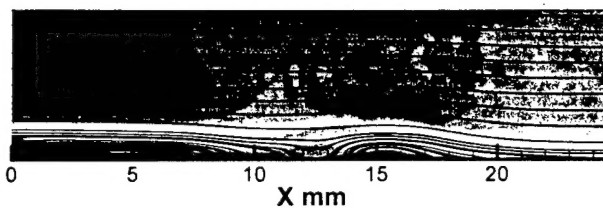

b) 15.4 % of input waveform, flap deflection = 22.5µm

c) 25.4 % of input waveform, flap deflection = 22.3µm

d) 35.4% of input waveform, flap deflection = 13.6 µm

e) 45.4 % of input waveform, flap deflection = -0.3µm

f) 55.4% of input waveform, flap deflection = -14.1µm
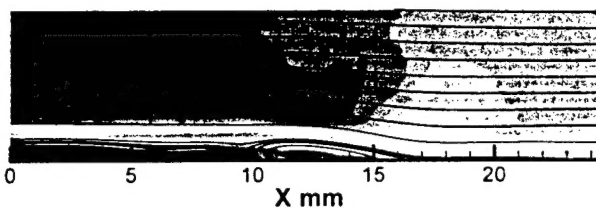
g) 65.4% of input waveform, flap deflection = -22.5µm

Fig. 11 Mean velocity profiles downstream of sudden expansion. Each image consists of realizations at a fixed phase shift relative to the actuator excitation signal. The vortex structure is apparent in this sequence of images. Excitation frequency is 200 Hz

the generation of a new convecting vortex. The convective speed of the vortex structures is approximately 2.0 m/s. Noting that the free stream velocity is 8.4 m/s, we see that the convective speed is approximately 24% of the free stream velocity.

Table 2 Conditionally Sampled Velocity Fields

% input waveform	Actuator tip deflection (μm)	Vortex location (mm)
5.4	14.1	8.9
15.4	22.5	9.8
25.4	22.3	10.7
35.4	13.6	11.9
45.4	-0.3	12.8
55.4	-14.1	14.0
65.4	-22.5	15.0

Computational Results

A computational investigation of this flow was performed in parallel with the experiments. A multiblock moving grid technique was employed in which grid distributions in each block were allowed to vary with time. In each grid block, a pressure-based flow solver is used on a structured body-fitted grid with a conservative interface treatment between grid blocks. The computations involved different flapping frequencies as well as fluid flow models (laminar, transitional and turbulent).

The methods for handling the moving boundary problems can be classified into Eulerian, Lagrangian and Eulerian-Lagrangian methods. The Lagrangian methods, which has been adopted in the present study, makes use of a moving grid in which a particular grid line is configured to conform to the shape of the moving flap, and thus grid and flap continually adapt to each other. A main issue in the model is the estimation of grid speed and metrics under the guidance of so-called Gemoetric Conservation Laws. For example, in the course of computation, one needs to consistently update the metrics to ensure the geometric conservation. In this study, a Jacobian transport equation is employed to update the cell Jacobian. There are several ways of writing the transport equations in curvilinear coordinates. In the present approach, the Cartesian velocities are used as the primary variables and the grid motion is accounted for through the contravariant velocity components in the momentum and other transport equations including the k-ε model. This approach maintains the strong conservation form of the governing equations.
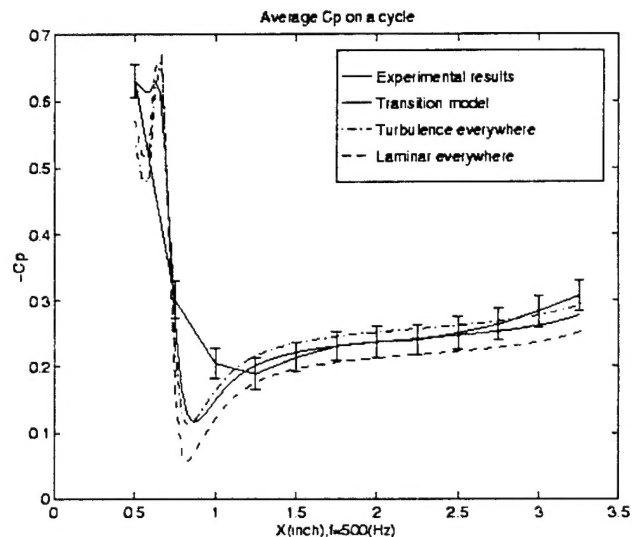

Fig. 12. Comparison of computed and measured surface pressures.

Similar issues exist for treating diffusion fluxes across the control volume faces for a non-uniform, non-orthogonal grid.

A combined k-ε and e^n model account for turbulence and transition effects. Details of the flow solver and turbulence modeling are given in the paper by He, et al. (2000). Computational results at different frequencies have been obtained and compared with the available experimental results. Comparisons between computations and measurements are shown in Figure 12. Qualitative agreement is observed. The solution was obtained based on the laminar-transitional-turbulent model. For the upper surface pressure coefficient, although numerical and experimental data are in qualitative agreement, the experimental seems to indicate a larger recirculation zone than computed. Results currently being obtained (after the end of this contract) indicate that the three dimensional shape of the actuating flap is important in obtaining accurate computed results.

Reports and Publications

The following is a list of reports and publications supported in whole or in part by this grant.

1. Chandrasekaran, V., Cain, A., Nishida, T., and Sheplak, M., "Dynamic Calibration Technique for Thermal Shear Stress Sensors with Variable Mean Flow," AIAA Paper 2000-0508, presented at the 38th AIAA Aerospace Sciences Meeting, Reno, NV, January 2000

2. Cain, A., Chandrasekaran, F., Nishida, T., and Sheplam, M., "Development of a Wafer-Bonded, Silicon Nitride Membrane Thermal Shear-Stress Sensor with Platinum Sensing Element," Technical Digest, Solid-State Sensor and Actuator Workshop, Hilton Head, SC, 300-303, June 2000.

3. Cain, A, "Static Characterization of a Micromachined Thermal Shear Stress Sensor," Masters Thesis, University of Florida, Gainesville, FL, 1999.

4. He, X., Senocak, I.,m Shyy, W., Thakur, S.S. and Gangadharan, S., "Evaluation of Laminar-Turbulent Transition and Equilibrium Near Wall Turbulence Models," Numerical Heat Transfer, Part A, Vol. 37, (2000) pp. 101-112.

5. He, X., Fuentes, C., Shyy, W., Lian, Y. and Carroll, B., "Computation of Transitional Flows around an Airfoil with a Movable Flap," AIAA Fluids 2000 Conference, Paper No. AIAA-2000-2240, June 19-22, (2000), Denver CO.

6. Lillberg, E., Kamkoti, R. and Shyy, W., "Computation of Unsteady Interaction between Viscous Flows and Flexible Structure with Finite Inertia," AIAA 38th Aerospace Sciences Meeting, Paper No. 2000-0142, (2000).

7. Shyy, W., Berg, M. and Ljungqvist, D., "Flapping and Flexible Wings for Biological and Micro Air Vehicles," Progress in Aerospace Sciences, Vol. 35, (1999) pp. 155-205.

8. Shyy, W., Klevebring, F., Nilsson, M., Sloan, J., Carroll, B. and Fuentes, C., "A Study of Rigid and Flexible Low Reynolds Number Airfoils," Journal of Aircraft, Vol. 36, (1999) pp. 523-529.

9. Shyy, W., He, X. and Thakur, S.S., "Jets and Free Stream Interaction Around a Low-Reynolds Number Airfoil Leading Edge," Numerical Heat Transfer, Part A, Vol. 35, (1999) pp. 891-902.

10. Carlos Fuentes, Xiong He, Bruce Carroll, Yongsheng Lian, and Wei Shyy, "Low Reynolds Number Flows Around an Airfoil with a Movable Flap – Part 1: Experiments" AIAA 2000-2239, Denver, CO, June 2000.